Quasi-monocrystalline silicon for low-noise end mirrors in cryogenic gravitational-wave detectors

Frank M. Kiessling [1] Peter G. Murray [2] Maya Kinley-Hanlon [2] Iryna Buchovska [1] Torunn K. Ervik [1,3]
Victoria Graham [2] Jim Hough,[2] Ross Johnston [2] Mike Pietsch [1] Sheila Rowan [2] Roman Schnabel [4] Simon C. Tait [2]
Jessica Steinlechner [2,4,5,6] and Iain W. Martin [2,*]

[1]*Leibniz-Institut für Kristallzüchtung, Max-Born-Str. 2, D-12489 Berlin, Germany*
[2]*SUPA, School of Physics and Astronomy, University of Glasgow, Glasgow G12 8QQ, United Kingdom*
[3]*National Institute of Occupational Health, Gydas vei 8, N-0363 Oslo, Norway*
[4]*Institut für Laserphysik und Zentrum für Optische Quantentechnologien, Universität Hamburg,*
Luruper Chaussee 149, D-22761 Hamburg, Germany
[5]*Maastricht University, Department of Gravitational Waves and Fundamental Physics, P.O. Box 616, 6200 MD Maastricht, Netherlands*
[6]*Nikhef, National Institute for Subatomic Physics, Science Park 105, 1098 XG Amsterdam, Netherlands*

Mirrors made of silicon have been proposed for use in future cryogenic gravitational-wave detectors, which will be significantly more sensitive than current room-temperature detectors. These mirrors are planned to have diameters of ≈50 cm and a mass of ≈200 kg. While single-crystalline float-zone silicon meets the requirements of low optical absorption and low mechanical loss, the production of this type of material is restricted to sizes much smaller than required. Here we present studies of silicon produced by directional solidification. This material can be grown as quasi-monocrystalline ingots in sizes larger than currently required. We present measurements of a low room-temperature and cryogenic mechanical loss comparable with float-zone silicon. While the optical absorption of our test sample is significantly higher than required, the low mechanical loss motivates research into further absorption reduction in the future. While it is unclear if material pure enough for the transmissive detector input mirrors can be achieved, an absorption level suitable for the highly reflective coated end mirrors seems realistic. Together with the potential to produce samples much larger than ≈50 cm, this material may be of great benefit for realizing silicon-based gravitational-wave detectors.

I. INTRODUCTION

Since 2015, Advanced LIGO [1] and Advanced Virgo [2] have detected many gravitational-wave signals. During the first two observing runs, ten binary black-hole mergers and one binary neutron-star merger were observed [3]. KAGRA, a third-generation detector, went online during the third observing run [4], by the end of which 90 additional gravitational-wave detections were reported [5,6], including signals originating from binary neutron stars, binary black holes, and possibly neutron-star–black-hole binaries.

Gravitational-wave detectors are km-scale interferometers which measure relative strains in space induced by passing gravitational waves. Highly reflective coated mirrors form the core components of these instruments, with the detector monitoring the relative separation of the mirrors in two perpendicular arms. Advanced LIGO and Advanced Virgo,

detectors of the second generation, operate at room temperature using mirror substrates made of fused silica (SiO_2). KAGRA is the first detector operating at cryogenic temperatures, designed to further reduce the thermal noise of the mirrors and their highly reflective coatings [7].

The mechanical loss, which determines the magnitude of the thermal noise, of fused silica increases by several orders of magnitude when cooling from room temperature to ≈20 K [8]. A different material is therefore required for the mirror substrates in a cryogenic detector. While KAGRA uses sapphire [9], other planned detectors such as LIGO Voyager [10] and the Einstein Telescope [11] are likely to use crystalline silicon.

To avoid heating from the laser light used for displacement sensing and to maintain cryogenic temperature, a mirror material with low optical absorption is essential. At wavelengths ≳1400 nm, high-purity, single-crystalline silicon can have a low optical absorption [12,13], when having a low level of doping and impurities (i.e., high resistivity), as the absorption scales down with the number of free carriers [14]. The purity level required for gravitational-wave detectors can be provided by silicon produced with the float-zone method. This type of silicon has also been shown to have low mechanical loss, resulting in low thermal noise, particularly at low temperatures [15]. However, the production of float-zone silicon with diameter of ≈20 cm is already very technically challenging

*Corresponding author: iain.martin@glasgow.ac.uk

and therefore the realization of larger diameters is unlikely [16].

From a thermal-noise perspective, Czochralski-grown (Cz) silicon, which can be grown in diameters of up to 45 cm [17], would also be a suitable material, but this type of silicon shows a higher level of impurities [18], resulting in a high absorption [13] which is incompatible with gravitational-wave detector mirrors. Magnetic field applied Czochralski (MCz) silicon, which has a reduced level of impurities [19], has been observed to show low absorption [20] and may be a promising way forward for gravitational-wave detection, if large enough substrate diameters can be produced.

Another way to produce silicon ingots in the required large sizes may be growth by directional solidification, which results in a quasi-monocrystalline material. In this process, single crystalline seed plates cut from a Cz-grown silicon boule cover the bottom of a Si_3N_4-coated quartz crucible, and polycrystalline silicon fragments are filled in on top of these plates. The standard industrial silicon feedstock charge of G6 ingots is about 800 kg with an ingot heights of 35 cm. "G" stands for the "generation" of directional solidification technology and the number contains information about the squared ingot size, e.g., six means that the ingot can be cut into 6×6 bricks for wafer slicing of standard solar cells with 156 mm $\times$ 156 mm in size. This G terminology is also used for furnaces and crucibles. Except for the seeds, the silicon is completely melted and then directionally solidified from the bottom of the melt upward. The process attempts to transfer the single-crystalline structure of the Cz seeds to the ingot. Dislocation formation and multiplication is still an unsolved problem in the crystallization of quasi-mono ingots.

In this article we present mechanical loss and optical absorption measurements of samples cut from a G2 quasi-monocrystalline silicon ingot. The mechanical loss of our test samples was found to be comparable to that of high-purity float-zone silicon, which is usually in the range of 10^{-8}–10^{-9}. However, the optical absorption at 1550 nm was found to be at a high level of several percent per centimeter, while the requirement is thought to be $\lesssim 5$–10×10^{-6} cm^{-1}. The high absorption was not unexpected because the material was doped and not optimized for low optical absorption. Further work on absorption reduction is of high interest. However, even with high absorption, quasi-monocrystalline silicon may be a candidate material for the "end test mass" (ETM) mirrors in gravitational-wave detectors, through which only very low laser power is transmitted.

II. QUASI-MONOCRYSTALLINE GROWTH TECHNIQUE AND SAMPLE PREPARATION

The quasi-monocrystalline silicon investigated here was originally grown for solar-cell production. The material was grown using two ⟨110⟩-oriented single crystalline seeds from Cz crystals, which were closely placed at the bottom of the G2-sized quartz crucible. The inner crucible walls were Si_3N_4 coated to prevent sticking with the silicon ingot. To obtain p-type material with a target resistivity of 0.9 Ω cm for solar cells, highly-boron-doped silicon wafer pieces with a specific resistivity of 0.0145 Ω cm together with silicon feedstock were placed on top of the seeds. The melting process of the
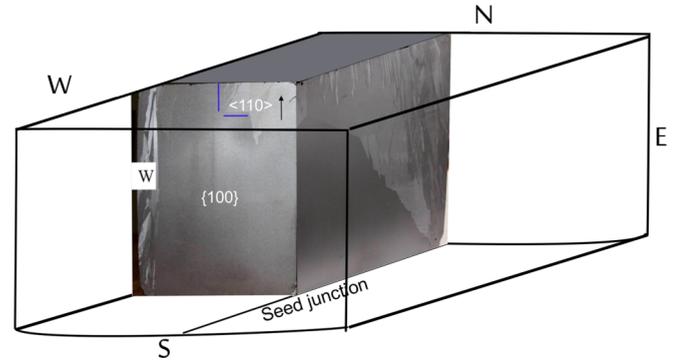

FIG. 1. Photo of the sandblasted G2 1/4 ingot sized $195 \times 195 \times 220$ mm^3. The drawing illustrates the position of the block in relation to the two seed plates (bottom plane). W-N-E-S are typically used markers to identify the position of the ingot to possible thermal asymmetries of the furnace, which might influence the growth process.

feedstock was carefully controlled until an equilibrium of the melt and the partially molten seeds was established. The ingot was directly solidified from the seeds to the top by a controlled temperature decrease of the molten silicon. The growth process was carried out in a G2-sized directional solidification furnace equipped with KRISTMAG® heater-magnet modules, which are able to produce heat and magnetic fields at the same time. A downward traveling 10 Hz oscillating magnetic field was applied to ensure a sufficient mixing of the melt by flow control. The average solidification velocity was determined to be 0.8–0.9 cm/h. More details about the use of the traveling magnetic field and growth velocity determination in this furnace were described by Linke *et al.* [21]. A quasi-monocrystalline ingot was obtained and then quartered. It is clearly seen from the depicted northwest quarter in Fig. 1 that this ingot is only partially single crystalline.

The crystal orientation of the seeds was mostly transferred to the growing ingot at the beginning of the solidification process. The single crystalline growth was strongly influenced by secondary grain growth from the crucible walls and formation of grains at twin boundaries (twins) [22] visible by different shades of gray due to different material orientations.

The selection of the samples investigated here was based on two main criteria. First, the material had to be monocrystalline, as required for the mirror substrates in gravitational-wave detectors, and second, the oxygen and carbon concentrations had to be as low as possible. Due to their different segregation behavior, the oxygen concentration decreases along the growth direction from the bottom to the top of the ingot while the carbon concentration increases [23,24]. These concentrations were measured in the overall characterization of the grown ingot on an adjacent longitudinal cut along the growth direction using FTIR spectroscopy (see Sec. V). In the sample selection area, the substitutional carbon concentration $[C_s] = 1$–3×10^{17} cm^{-3} and the interstitial oxygen concentration $[O_i] = 2$–3×10^{17} cm^{-3} were measured at a scan distance of 1 cm.

Two single-crystalline samples of $40 \times 15 \times 15$ mm^3 (named "small QM cuboid") and $80 \times 80 \times 15$ mm^3 were cut from the central part, as indicated in Fig. 2. From the
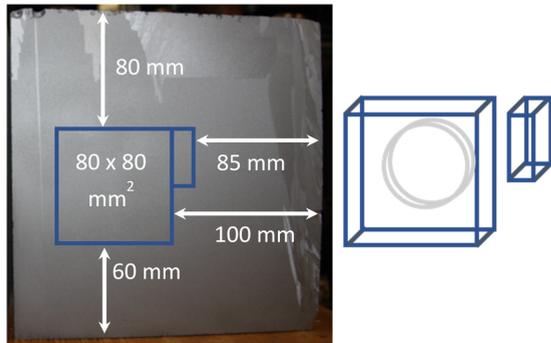
FIG. 2. (left) Sample position marked on a photo of the {100} vertical cut of a G2 1/4 ingot. (right) Drawing of the final ø 50.8 × 5-mm-thick disk (gray: QM disk) inside the bigger single crystalline cuboid, and the position of the smaller sample (small QM cuboid) for absorption measurements.

bigger cuboid, a 50.8-mm-diameter × 5-mm-thick disk was cut (named "QM disk"). Both samples were polished to be used for optical absorption and mechanical-loss measurements, respectively.

III. MECHANICAL-LOSS MEASUREMENTS

Mechanical loss is a measure of the magnitude of internal friction in a material. The thermal displacement noise arising from a mirror substrate in a gravitational-wave detector (in m/$\sqrt{\text{Hz}}$) is proportional to the square root of the mechanical loss of the mirror material. The mechanical loss of a number of resonant modes of the $\langle 100 \rangle$-oriented QM disk was measured using a gentle nodal suspension (GeNS) system [25], and compared with the mechanical loss of a float-zone $\langle 111 \rangle$ silicon sample of the same dimensions (named "FZ disk"). Previous work by Nawrodt *et al.* on similar geometries of silicon substrates showed almost identical loss between 30 and 200 K for these different crystal orientations [26].

Figure 3 shows a photo of the setup used for cryogenic mechanical loss measurements. The disk (top of the picture) being measured was balanced on a silicon spherical lens with a radius of curvature of 60.44 mm, where it balanced freely throughout the measurements. The cryostat chamber was evacuated to pressures below 10^{-5} mbar, and the mechanical resonances of the samples were excited via comb-shaped capacitor exciter plates, visible underneath the bottom-left of the substrate in Fig. 3, placed ≈1 mm away from the surface of the disks. The resonant modes of the disks are excited by applying a high-voltage ac signal to the exciter plate, sweeping slowly over the frequency of the mode. After a mode is excited the excitation voltage is turned off, and the vibration of the sample is left to decay. The motion of the sample is measured by reflecting a laser beam from the face of the sample onto a split-photodiode sensor, which provides a signal proportional to the amplitude of the motion. The loss $\phi(\omega_0)$ of the resonant mode of angular frequency ω_0 is calculated from the exponential decay of the excited amplitude, which follows the form
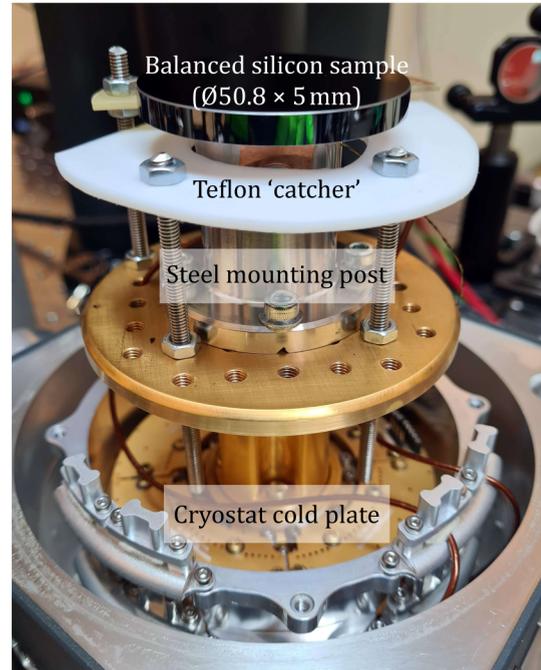
$$A(t) = A_0 e^{[-\phi(\omega_0)\omega_0 t/2]}, \tag{1}$$

FIG. 3. Image of the $\langle 100 \rangle$-oriented QM disk balanced on top of a rounded silicon lens inside the 10×10 cm^2 experimental chamber of the Montana Instruments s100 Cryostation.

where $A(t)$ is the amplitude at a time t and A_0 is the initial amplitude after the excitation is turned off.

Figure 4 shows the resonant mode shapes of six resonant modes (14.7, 17.8, 36.0, 36.0, 60.1, and 87.8 kHz) at room temperature of the QM disk. For the FZ disk, the mode frequencies differ due to the difference in crystal orientation.

A. Mechanical loss at room temperature

Initially, the mechanical loss of the QM and FZ disks was measured at room temperature. The loss of each resonant mode was measured multiple times, with the average loss calculated and the error taken as the standard deviation. Each disk was rebalanced on the nodal support several times and the loss measurements repeated. For each resonant mode we present the lowest loss obtained from the repeated suspensions, as is standard in loss measurements. The results are shown in Fig. 5 (see values at 290 K for room temperature measurements).

For both disks, all measured losses are below 1×10^{-6}. For the modes at 14.75 and 17.85 kHz, the room-temperature loss of the QM disk is lower than that of the two lowest resonance frequencies of the FZ disk, while for the modes around 36 kHz, the loss of the FZ disk is lower. For the QM disk, also a mode at about 60 kHz was measured which shows a loss similar to that measured at about 36 kHz on the same sample.

B. Mechanical loss at cryogenic temperatures

After the initial room-temperature measurements, the mechanical loss of the QM and FZ disks was measured at cryogenic temperatures. In turn they were individually placed
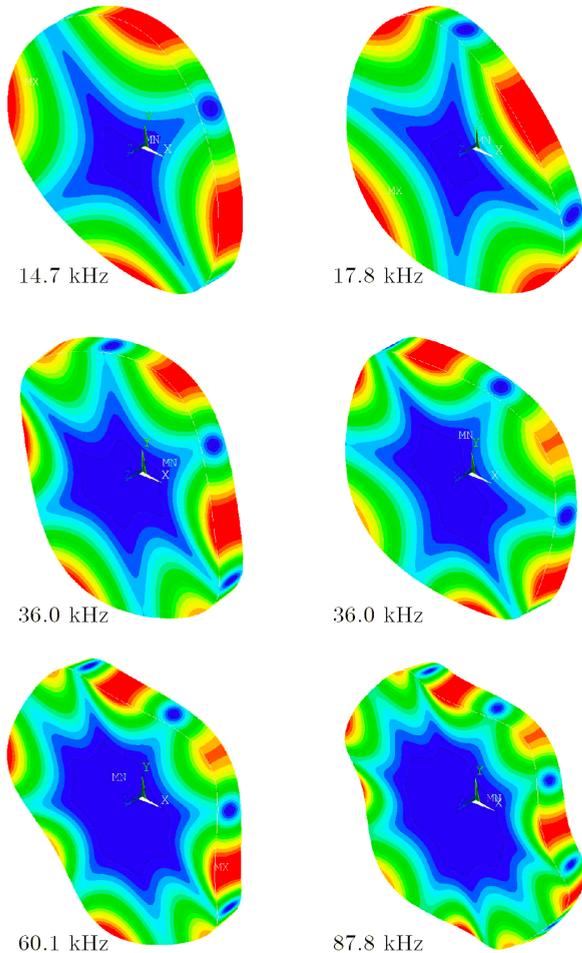
14.7 kHz

17.8 kHz

36.0 kHz

36.0 kHz

60.1 kHz

87.8 kHz

FIG. 4. Total surface deformation of the resonance modes of the ⟨100⟩-orientated QM disk, calculated using finite-element analysis. The blue corresponds to regions of least motion and the red to regions of greatest motion.

inside a small pulse-cooled cryostat [27] capable of cooling down to 4 K. The cryostat housed a GeNS, similar to the one used for room-temperature measurements, with an identical silicon spherical lens held in a recess in the top of a stainless-steel post. A temperature cycle of the cryostat was carried out with calibrated temperature sensors mounted on the sample and on the post close to the silicon lens. This allowed a temperature calibration curve to be created so that the sample temperature could be determined from the temperature of the post. The temperature sensor on the sample was removed for mechanical loss measurements.

The mechanical losses of several resonant modes of both the QM and FZ disks were measured over a range of temperatures between 20 and 290 K. The procedure of several repeated measurements providing an average loss with error bars given by the standard deviation was the same as for the room-temperature measurements. The QM disk was measured three times over the full temperature range, with the sample being rebalanced on the nodal support each time, to check for repeatability. Due to the time constraints of a full mechanical loss run over the entire temperature range (≈1 month), the FZ disk was only able to be measured once before it was needed for another study.

Figure 5 shows the mechanical loss as a function of temperature for four resonant modes of both samples. The mechanical loss of the QM disk shows a very similar trend to the losses measured for the FZ disk. For some resonant modes, the mechanical loss is lower than that of the FZ disk. At 20 K the lowest mechanical loss measured on the QM disk was 2.6×10^{-8} at 17.8 kHz which is marginally higher than the lowest loss measured at 36.81 kHz on the FZ disk of $\approx 2 \times 10^{-8}$. At 120 K the losses of all the modes measured were below $\approx 2 \times 10^{-7}$. The lowest loss measured on the QM disk ($\approx 1.8 \times 10^{-8}$) was more than a factor of two lower than the lowest loss of $\approx 4.3 \times 10^{-8}$ measured on the FZ disk.

The mechanical loss of the first two modes at 14.75 and 17.85 kHz of the QM disk was lower than that of the two higher-frequency resonance modes at 36.01 and 60.21 kHz, whereas the opposite was true for the FZ disk. This may be related to the different crystal orientation of the samples as the QM disk was ⟨100⟩ orientated and the FZ disk ⟨111⟩ orientated. These results are nevertheless still very promising for the quasi-monocrystalline material, making it potentially relevant for use in cryogenic gravitational-wave detectors.

In the following section we also present measurements of the optical absorption of this quasi-monocrystalline material, which is also significant in determining a materials suitability for gravitational-wave detector mirrors.

IV. OPTICAL ABSORPTION MEASUREMENTS

The optical absorption of the quasi-monocrystalline silicon sample (the small QM cuboid in Fig. 2, ≈40 mm in length) was measured by using photothermal common-path interferometry (PCI) [28]. The PCI technique exploits thermally induced optical length changes, created by a strong pump laser beam at the wavelength of interest due to optical absorption. The thermal effect, read out by a weak probe beam different in wavelength, is directly proportional to the absorption of the substrate. The setup can be calibrated by using a substrate of known absorption, in our case made of fused silica.

An optical chopper is used to modulate the pump beam, enabling phase information relative to this modulation to be obtained, in addition to the amplitude of the thermal effect. The phase is determined by the thermal diffusion of the material and the geometric parameters of the laser beams.

Based on the thermal diffusivity and the thermo-optic parameters of the investigated substrate, e.g., our silicon crystal, an additional factor is used to scale the amplitude signal to the signal of fused silica. For silicon (and the measurement/setup parameters used in this study), this scaling factor is 0.42 for a phase of $-8.5°$. More detail about the measurement procedure can be found in literature [28] and on the company website [29].

Figure 6 shows the optical absorption measured at 1550 nm (using a probe laser of wavelength 1620 nm) as a function of position along the length of the small QM cuboid. Measurements starting at three different positions on the surface were made, resulting in parallel scans through the sample, represented by the three different colors and line styles in
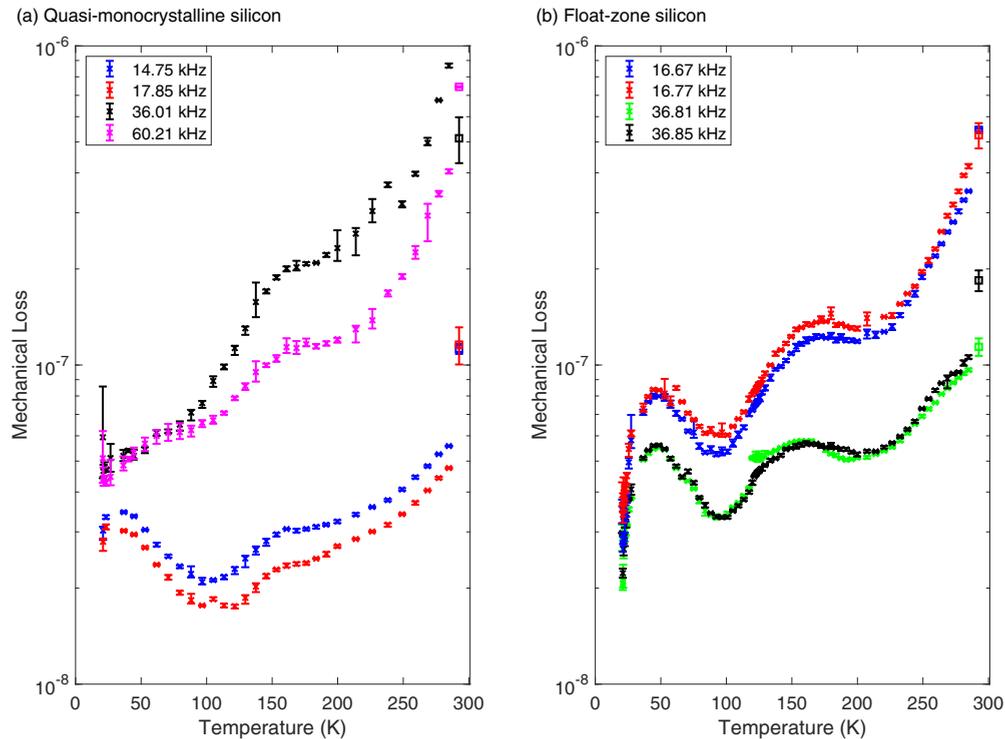
FIG. 5. Mechanical loss as a function of temperature, from 4 to 300 K, of the 50.8-mm-diameter $\times$ 5-mm-thick QM disk (left) and FZ disk (right) samples.

Fig. 6(a). The vertical dashed lines mark the surface positions for the measurement represented by the green, dashed line.

For all three positions, the absorption shows a peak near the front surface (*x* position of around 10–15 mm) and decreases towards the back surface. To test if the peak near the front surface could be an artifact of the measurement technique, the sample was turned around and the measurement was repeated at two new positions [pink and purple lines in Fig. 6(b)]. These measurements show the absorption peak at the back of the sample, indicating that one end of the sample does indeed have higher absorption than the other. Possible correlations with impurities are discussed in Sec. V. For comparison, the horizontal black line shows an absorption level of $\approx 9.6\%$ cm^{-1} estimated from a simple transmission measurement.

Figures 6(c) and 6(d) show the phase signals corresponding to the absorption scans of the same colors in Figs. 6(a) and 6(b), where the red line indicates the phase expected for crystalline silicon.

From these measurements, we conclude an absorption of several 10% cm^{-1} at one end of the sample, and between ≈ 5–10% cm^{-1} throughout the remainder of the bulk of the sample, varying with position. An absorption of $\approx 5\%$ cm^{-1} is consistent with a boron-doping level of 0.9 Ω cm [13].

Nonlinear absorption in silicon (arising from two photon absorption, and free carrier absorption due to carriers produced by two photon absorption) can result in a power-dependent absorption signal, potentially masking the intrinsic absorption. To check for this, measurements were repeated at different pump power of ≈ 300 mW and ≈ 840 mW, instead of ≈ 600 mW as initially used. No change in the measured absorption was observed, indicating that nonlinear absorption

does not make a significant contribution to the measured absorption in this measurement regime. This agrees with the low absorption contribution calculated from the nonlinear (two-photon absorption) coefficients [30].

This absorption level is far too high for this material to be used (for transmitted optics) in gravitational-wave detectors. However, this material had not been optimized for low optical absorption, which would be the next obvious development step. In the following section, further analysis of possible absorption sources is presented.

V. IMPURITY CHARACTERIzATION

After the optical absorption measurements were carried out on the ≈ 40 mm small QM cuboid, the minority carrier lifetime and the concentration of carbon and oxygen were determined to identify possible origins for the absorption. To carry out these examinations the small QM cuboid was cut lengthwise and polished on both sides using a chemo-mechanical polishing technique to a final thickness of 2510 μm. Existing markings on one end face (the marked side is set equal to the zero point) were retained to enable the measurements made in the longitudinal direction to be assigned true to location. Following the polishing, elevations were found close to the marked side. Using a light microscope the elevations were determined to be typical in shape and size for silicon carbide (SiC) inclusions, see Fig. 7. If this estimation is true, then a carbon concentration close to the solubility limit of carbon in silicon is also to be expected in the surrounding material. The solubility limit in liquid silicon at melting temperature is 4.5×10^{17} cm^{-3} [31].
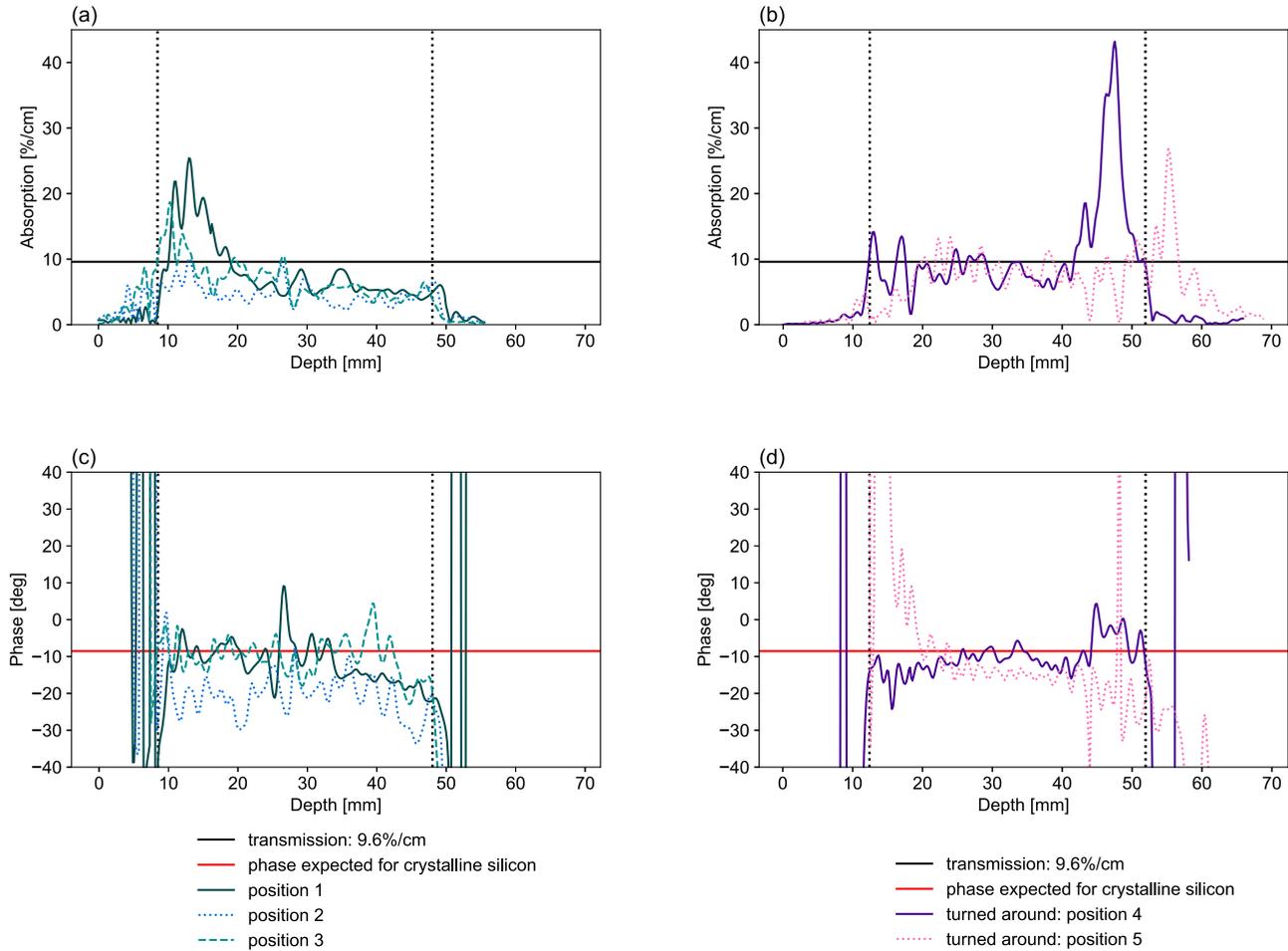
FIG. 6. (a) Optical absorption along the ≈40-mm-long small QM cuboid for entering the sample at three different positions indicated by the different colors and line styles. The dotted vertical lines indicate the surface positions for the measurements shown by the green, dashed line (the position of the sample front surface slightly varied between measurements). (b) Optical absorption scans through the sample at two different positions after turning the sample back surface to the front. Panels (c) and (d) show the corresponding phase signals of those measurements. Outside the sample, the signal is meaningless: while the absorption signal becomes approximately zero, the phase shows large oscillations.

Exceeding the solubility limit in the melt leads to the formation of SiC particles, which can then be trapped at the growth interface as second phase particles and manifest themselves as inclusions. This formation and capturing process is well known [23,24]. The trapping of the SiC particles in the middle of the growth process indicates insufficient mixing and can be avoided. This surface structuring is found only in the first quarter of the ≈40-mm-long sample, i.e., in the range from 0 to about 10 mm, while on the remaining surface of the sample almost no inclusions are detectable with the light-field microscope (Fig. 7).

Interstitial oxygen O_i and substitutional carbon C_S in silicon are associated with typical absorption lines at 1107 and 605 cm^{-1}, respectively. The absorption spectra were measured axially along the sample by Fourier-transform infrared spectroscopy (FTIR) using a Bruker IFS 66 V under vacuum. Two measuring rows by different measuring point dimensions were carried out. Both measuring rows started from the marked side and continued beyond the sample. The first measuring row was carried out in a measuring distance of

1 mm with an aperture of 2 mm which is the smallest possible with the apparatus used, while the second measuring row was carried out for reasons of smoothing with an aperture of 3.5 mm in diameter with the same measuring distance of 1 mm.

In Fig. 8, the carbon concentration is shown along the sample length starting from the marked side (zero) with optically observed inclusions. This marked side corresponds to the side with higher absorption in Fig. 6. Both curves, measured with aperture 2 mm (black) and aperture 3.5 mm (red), show the same shape and by use of the smaller aperture the measuring values do not make sense (measuring error amounts to approximately 5%). This might be due to scatter or/and absorption in the SiC inclusions.

Figure 9 shows analogously the oxygen concentration along the sample length measured with apertures of 2 mm (black) and 3.5 mm (red), both showing an increase in the oxygen concentration from 2×10^{16} to 3×10^{17} cm^{-3}. During the directionally solidification growth, the oxygen concentration decreases in the direction of solidification in the ingot
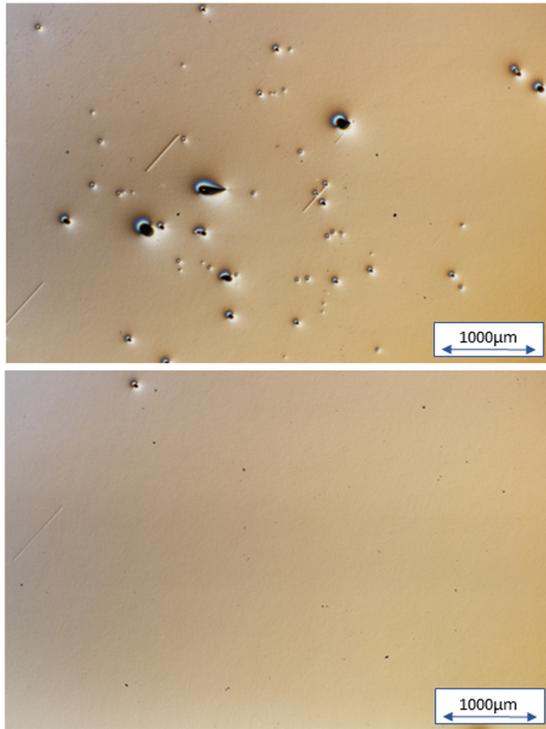
FIG. 7. Typical light microscopic image of SiC inclusions near the surface in the range of 0–10 mm of the sample (top), while almost no superficial features can be seen on the rest of the sample (bottom).

caused by the dominance of evaporation over dissolution and a segregation coefficient[1] larger than one [24]. Consequently, the sample orientation in the block in respect to the growth direction can be determined: the silicon at position 40 solidified first, named additionally with "bottom" in Figs. 8 and 9. This also has consequences for the quality of the 2 inch disk

———————
[1]The segregation coefficient is defined as the concentration ratio of an impurity in a solid to this impurity in a liquid.
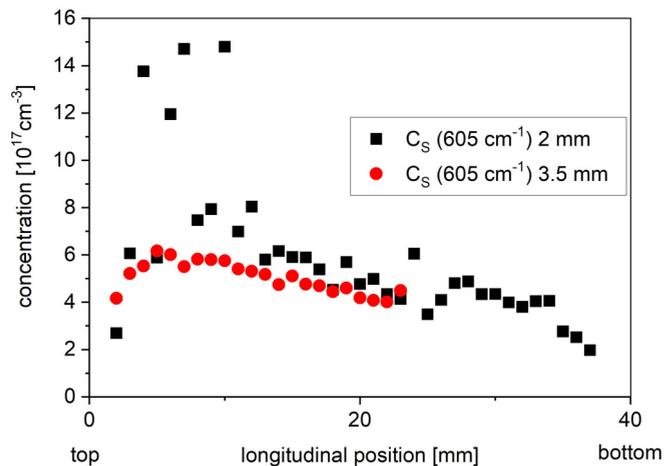

FIG. 8. FTIR measurement of [C_S] in longitudinal direction with different apertures: red 3.5 mm and black curve 2 mm.
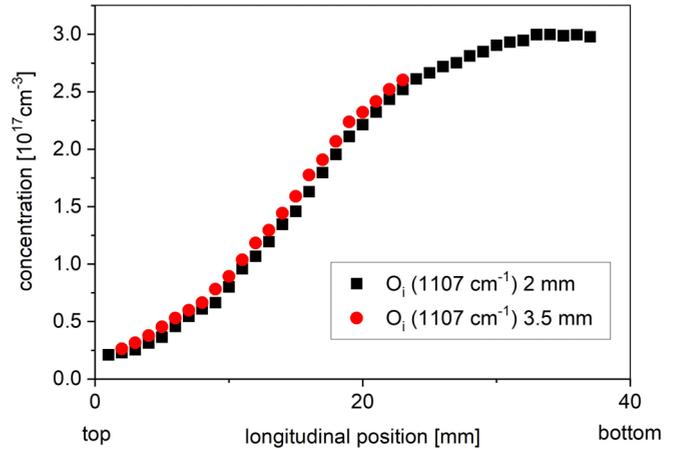

FIG. 9. FTIR measurement of [O_i] in longitudinal direction with different apertures: red 3.5 mm and black curve 2 mm.

used for mechanical loss measurements, where SiC inclusions should be present only in a rim area.

Measuring the interstitial oxygen and substitutional carbon concentration in smaller steps (1 mm) compared with the initial survey (see Sec. II) measurement with a distance of 1 cm, a locally unexpected lower interstitial oxygen concentration was detected in the area with significantly higher absorption, see Figs. 9 and 6. The absorption peak at this one end of the sample can neither be explained by the measured interstitial oxygen (too low) nor by the substitutional carbon (too homogeneous) concentrations. This local effect can probably be attributed to defect interaction. Capture of SiC particles in the silicon matrix can lead to dislocation formation. The locally higher dislocation density can getter higher amounts of oxygen, potentially leading to the formation of oxygen precipitates during ingot cooling. To investigate the nature of this phenomena minority-carrier lifetime was performed by the microwave-detected photoconductivity (MDP) method [32] on this polished nonpassivated longitudinal sample. Figure 10 shows that the carrier lifetime is significantly reduced in the area of the SiC inclusions but shows otherwise typical lifetimes. The reduced lifetime might be due to a higher density of oxygen precipitates [23,33]. It can be assumed that the increased absorption at one end of the sample is due to defect interaction initiated by SiC inclusion. This formation of SiC can be avoided if the carbon input is significantly reduced in an optimized growth process.

VI. DISCUSSION

Our results show that quasi-monocrystalline silicon can have very low mechanical loss, similar to the loss observed in high-purity float-zone silicon. This suggests the material could meet the thermal noise requirements for cryogenic gravitational-wave detectors, while also being available in the large diameters required (and beyond).

For example, G7-type mono-like silicon ingots can be produced, the mass of which reaches 1200 kg with a square width of 1151 mm and a height of 390 mm [34]. However, the single-crystal area ratio and dislocation are the main problems associated with the mono-like technique. It has been shown
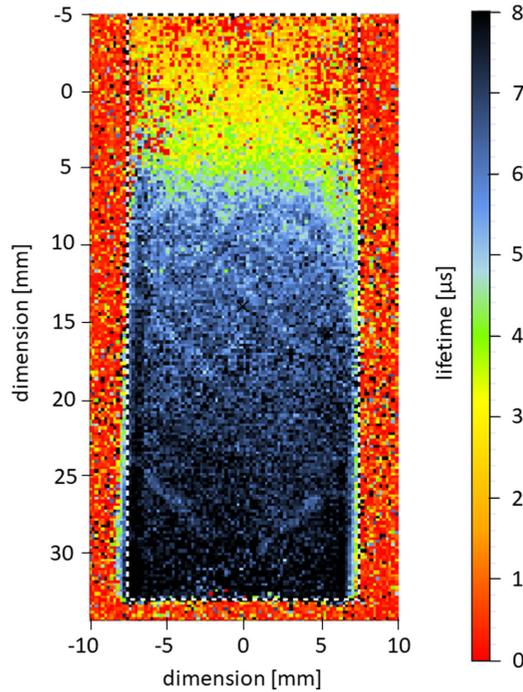
FIG. 10. Measurements of minority-carrier lifetime on the now thinned $\approx$40-mm-small QM cuboid (used previously for absorption measurements). The low values at the marked edge (here position -5 on the vertical axis) correspond to the high-absorption end.

in smaller ingots that dislocation gliding and propagation can be effectively controlled using $\langle 110 \rangle$-oriented seeds and the average {100} single-crystal proportion has been increased over 90%. An overview about seed-assisted growth of quasi-monocrystalline silicon ingots and its challenges is given in Ref. [35]. It should be noted that the mechanical loss was measured from a sample in a single-crystalline region of the quasi-monocrystalline ingot. Further development of the growth technique is likely to be required to ensure an area of monocrystalline material large enough for a gravitational-wave detector test mass to be produced.

The optical absorption of our test material was found to be significantly higher than the value, of $\lesssim 5$–10×10^{-6} cm^{-1}, usually thought to be required for a gravitational-wave detector mirror. However, it is interesting to note that only the "input test masses" (ITMs) in the arm cavities of a gravitational-wave detector are required to transmit significant laser power. The "end test masses" (ETMs), however, do not have significant power transmitted through them and somewhat higher absorption can therefore be tolerated in comparison to the ITMs. In a typical gravitational-wave detector configuration— with an ITM reflectivity of $\approx$99.5% and an ETM reflectivity of $\approx$99.9995%—the higher reflectivity of the ETM coating results in a factor of $\approx$200 less laser power being transmitted through the ETM than through the ITM. Therefore, we can tolerate a factor of 200 higher absorption in the ETM (resulting in ≈ 1–2×10^{-3} cm^{-1} tolerable absorption).

The silicon investigated here was specifically boron doped with a resistivity of 0.9 Ω cm in order to achieve the desired resistance for solar cells and was not grown specifically with a view to a low level of (unintended) impurities poten-

tially increasing the absorption at wavelengths relevant for gravitational-wave detectors. The absorption throughout the majority of the length of the sample, of $\approx$5%–10% cm^{-1} ($\approx$5–10×10^{-2} cm^{-1}), was consistent with the absorption estimated from the corresponding carrier concentration [36,37]. One end of the sample showed a higher absorption which may be due to a higher concentration of carriers. An absorption reduction of about two orders of magnitude would be required to make it a suitable ETM material.

If undoped and high-purity feedstock silicon is used, it is to be expected that the purity of the quasi-monocrystalline material can be significantly increased. Nevertheless B, Al, and P, other metal impurities, such as Fe, Co, Ni, and Cr, are quite common in quasi-monocrystalline silicon. They mainly come from the crucible, its coating materials and the hot zone of the furnace. To increase the resistivity and hence reduce the bulk absorption by orders of magnitude, the impurity sources must be eliminated. The standard crucible can be replaced by a high-purity fused silica crucible coated with high-purity Si$_3$N$_4$ layers. The oxygen and carbon concentrations in the material get significantly lowered by an improved design of the hot zone with an optimized gas flow. Defect engineering includes an optimized growth process and subsequent annealing of the ingot dissolving precipitates and thermal donors that are present in the as-grown material. Whether directionally solidified silicon can finally meet the absorption requirements of a mirror has to be investigated.

VII. SUMMARY

Quasi-monocrystalline silicon grown by directional solidification shows significant promise of being able to meet the size and thermal noise requirements for cryogenic GWD mirrors. The optical absorption of the specific material studied here was high, as expected due to the doping, but it appears likely that with the use of pure feedstock, the absorption can be significantly reduced, at least to the point where this material would be suitable for use as an ETM mirror substrate in cryogenic gravitational-wave detectors. Further research is required to determine if it may be possible to reduce the absorption sufficiently to allow this material to be used as an ITM mirror substrate. Another option may be increasing the size of the ETMs to beyond $\approx$50 cm by using quasi-monocrystalline silicon which is available in larger diameters. Combining this with significantly smaller ITMs, similar to the configuration planned for Advanced Virgo upgrades [38], would then allow for different types of (pure) silicon potentially to be used as ITMs.

Loss and absorption datasets presented in this paper can be accessed at [39].

[1] B. P. Abbott, R. Abbott, T. D. Abbott, M. R. Abernathy, F. Acernese, K. Ackley, C. Adams, T. Adams, P. Addesso, R. X. Adhikari *et al.* (LIGO Scientific Collaboration and Virgo Collaboration), GW150914: The Advanced LIGO Detectors in the Era of First Discoveries, Phys. Rev. Lett. **116**, 131103 (2016).

[2] F. Acernese *et al.*, Advanced Virgo: A second-generation interferometric gravitational wave detector, Classical Quantum Gravity **32**, 024001 (2015).

[3] B. P. Abbott, R. Abbott, T. D. Abbott, S. Abraham, F. Acernese, K. Ackley, C. Adams, R. X. Adhikari, V. B. Adya, C. Affeldt, (LIGO Scientific Collaboration and Virgo Collaboration) *et al.*, GWTC-1: A Gravitational-Wave Transient Catalog of Compact Binary Mergers Observed by LIGO and Virgo during the First and Second Observing Runs, Phys. Rev. X **9**, 031040 (2019).

[4] Y. Aso, Y. Michimura, K. Somiya, M. Ando, O. Miyakawa, T. Sekiguchi, D. Tatsumi, and H. Yamamoto (KAGRA Collaboration), Interferometer design of the KARGA gravitational wave detector, Phys. Rev. D **88**, 043007 (2013).

[5] R. Abbott, T. D. Abbott, S. Abraham, F. Acernese, K. Ackley, A. Adams, C. Adams, R. X. Adhikari, V. B. Adya, C. Affeldt, (LIGO Scientific Collaboration and Virgo Collaboration) *et al.*, GWTC-2: Compact Binary Coalescences Observed by LIGO and Virgo during the First Half of the Third Observing Run, Phys. Rev. X **11**, 021053 (2021).

[6] LIGO Scientific Collaboration, Virgo Collaboration, and KAGRA Collaboration, GWTC-3: Compact binary coalescences observed by LIGO and Virgo during the second part of the third observing run, arXiv:2111.03606.

[7] G. M. Harry, A. M. Gretarsson, P. R. Saulson, S. E. Kittelberger, S. D. Penn, W. J. Startin, S. Rowan, M. M. Fejer, D. R. M. Crooks, G. Cagnoli, J. Hough, and N. Nakagawa, Thermal noise in interferometric gravitational wave detectors due to dielectric optical coatings, Classical Quantum Gravity **19**, 897 (2002).

[8] M. E. Fine, H. van Duyne, and N. T. Kenney, Low-temperature internal friction and elasticity effects in vitreous silica, J. Appl. Phys. **25**, 402 (1954).

[9] E. Hirose, D. Bajuk, G. Billingsley, T. Kajita, B. Kestner, N. Mio, M. Ohashi, B. Reichman, H. Yamamoto, and L. Zhang, Sapphire mirror for the KAGRA gravitational wave detector, Phys. Rev. D **89**, 062003 (2014).

[10] R. X. Adhikari, K. Arai, A. F. Brooks, C. Wipf, O. Aguiar, P. Altin, B. Barr, L. Barsotti, R. Bassiri, A. Bell *et al.*, A cryogenic silicon interferometer for gravitational-wave detection, Classical Quantum Gravity **37**, 165003 (2020).

[11] ET Editorial Team, Design Report Update 2020 for the Einstein Telescope (2020), https://apps.et-gw.eu/tds/?content=3&r=17245.

[12] M. A. Green and M. J. Keevers, Optical properties of intrinsic silicon at 300 K, Prog. Photovoltaics **3**, 189 (1995).

[13] J. Degallaix, R. Flaminio, D. Forest, M. Granata, C. Michel, L. Pinard, T. Bertrand, and G. Cagnoli, Bulk optical absorp-

[13] tion of high resistivity silicon at 1550 nm, Opt. Lett. **38**, 2047 (2013).

[14] R. R. Vardanyan, V. K. Dallakyan, U. Kerst, and C. Boit, Modeling free carrier absorption in silicon, J. Contemp. Phys. (Arm. Acad. Sci.) **47**, 73 (2012).

[15] D. F. McGuigan, C. C. Lam, R. Q. Gram, A. W. Hoffman *et al.*, Measurements of the mechanical Q of single-crystal silicon at low temperatures, J. Low Temp. Phys. **30**, 621 (1978).

[16] W. von Ammon, FZ and CZ crystal growth: Cost driving factors and new perspectives, Phys. Status Solidi A **211**, 2461 (2014).

[17] Z. Lu and S. Kimbel, Growth of 450 mm diameter semiconductor grade silicon crystals, J. Cryst. Growth **318**, 193 (2011).

[18] *Handbook of Semiconductor Manufacturing Technology*, 2nd ed., edited by R. Doering and Y. Nishi (CRC Press, Boca Raton, 2008).

[19] *Springer Handbook of Electronic and Photonic Materials*, Springer Handbooks, edited by S. Kasap and P. Capper (Springer, Cham, 2017).

[20] I. Martin, A. Bell, J. Steinlechner, P. Murray, J. Hough, R. Schnabel, R. Robie, S. Rowan, S. Tait, A. Markosyan, M. Fejer, E. Gustafson, C. Wipf, and R. Adhikari, Development of silicon mirrors and coatings (2017), https://dcc.ligo.org/LIGO-G1700882/public.

[21] D. Linke, N. Dropka, F. M. Kiessling, M. König, J. Krause, R.-P. Lange, and D. Sontag, Characterization of a 75 kg multicrystalline Si ingot grown in a KRISTMAG®-type G2-sized directional solidification furnace, Sol. Energy Mater. Sol. Cells **130**, 652 (2014).

[22] K. Kutsukake, T. Abe, N. Usami, K. Fujiwara, K. Morishita, and K. Nakajima, Formation mechanism of twin boundaries during crystal growth of silicon, Scr. Mater. **65**, 556 (2011).

[23] H. J. Möller, T. Kaden, S. Scholz, and S. Würzner, Improving solar grade silicon by controlling extended defect generation and foreign atom defect interactions, Appl. Phys. A: Mater. Sci. Process. **96**, 207 (2009).

[24] F.-M. Kiessling, F. Büllesfeld, N. Dropka, Ch. Frank-Rotsch, M. Müller, and P. Rudolph, Characterization of mc-Si directionally solidified in travelling magnetic fields, J. Cryst. Growth **360**, 81 (2012).

[25] E. Cesarini, M. Lorenzini, E. Campagna, F. Martelli, F. Piergiovanni, F. Vetrano, G. Losurdo, and G. Cagnoli, A "gentle" nodal suspension for measurements of the acoustic attenuation in materials, Rev. Sci. Instrum. **80**, 053904 (2009).

[26] R. Nawrodt, A. Zimmer, T. Koettig, C. Schwarz, D. Heinert, M. Hudl, R. Neubert, M. Thürk, S. Nietzsche, W. Vodel, P. Seidel, and A. Tünnermann, High mechanical Q-factor measurements on silicon bulk samples, J. Phys.: Conf. Ser. **122**, 012008 (2008).

[27] Montana Instruments Cryostation s100; https://www.montanainstruments.com.

[28] A. Alexandrovski, M. Fejer, A. Markosian, and R. Route, Photothermal common-path interferometry (PCI): New developments, in *Solid State Lasers XVIII: Technology and Devices*, edited by W. A. Clarkson, N. Hodgson, and R. K. Shori, International Society for Optics and Photonics (SPIE, 2009), Vol. 7193, pp. 79–91.

[29] Stanford Photo-Thermal Solutions; www.stan-pts.com.

[30] *Handbook of Silicon Photonics*, edited by Laurent Vivien and Lorenzo Pavesi (CRC Press, Boca Raton, 2013).

[31] F. Durand and J. C. Duby, Carbon solubility in solid and liquid silicon—a review with reference to eutectic equilibrium, J. Phase Equilib. **20**, 61 (1999).

[32] B. Berger, N. Schüler, S. Anger, B. Gründig-Wendrock, J. R. Niklas, and K. Dornich, Contactless electrical defect characterization in semiconductors by microwave detected photo induced current transient spectroscopy (MD-PICTS) and microwave detected photoconductivity (MDP), Phys. Status Solidi A **208**, 769 (2011).

[33] H. J. Möller, L. Long, M. Werner, and D. Yang, Oxygen and carbon precipitation in multicrystalline Si, Phys. Status Solidi A **171**, 175 (1999).

[34] C. W. Lan, C. F. Yang, A. Lan, M. Yang, A. Yu, H. P. Hsu, B. Hsu, and C. Hsu, Engineering silicon crystals for photovoltaics, CrystEngComm **18**, 1474 (2016).

[35] P. Wang, C. Cui, D. Yang, and X. Yu, Seed-assisted growth of cast-mono silicon for photovoltaic application: Challenges and strategies, Sol. RRL **4**, 1900486 (2020).

[36] W. R. Thurber, R. L. Mattis, Y. M. Liu, and J. J. Filliben, Resistivity-dopant density relationship for boron-doped silicon, J. Electrochem. Soc. **127**, 2291 (1980).

[37] C.-Y. Tsai, Interband and intraband absorption coefficients of silicon: Theoretical frameworks and formulations, IEEE J. Sel. Top. Quantum Electron. **26**, 1 (2020).

[38] J. Baird and M. Barsuglia, Fine-tuning the optical design of the advanced Virgo+ gravitational-wave detector using binary-neutron star signals, Galaxies **8**, 86 (2020).

[39] http://dx.doi.org/10.5525/gla.researchdata.1344.